Chemical Engineering Science 273 (2023) 118638

Contents lists available at ScienceDirect

Chemical Engineering Science

journal homepage: www.elsevier.com/locate/ces

Efficiently electrochemical CO_2 reduction on molybdenum-nitrogen-carbon catalysts with optimized p-block axial ligands

Yingnan Liu[a], Dashuai Wang[a,b,*], Bin Yang[a,b], Zhongjian Li[a,b], Xianyun Peng[b], Zhibin Liu[b], Libin Zeng[b], Tao Zhang[d], Raul D. Rodriguez[e], Lecheng Lei[a,b], Yang Hou[a,b,c,*]

[a] Key Laboratory of Biomass Chemical Engineering of Ministry of Education, College of Chemical and Biological Engineering, Zhejiang University, Hangzhou 310027, China
[b] Institute of Zhejiang University - Quzhou, Quzhou 324000, China
[c] Donghai Laboratory, Zhoushan, China
[d] Ningbo Institute of Materials Technology & Engineering, University of Chinese Academy of Sciences, Ningbo 315200, China
[e] Tomsk Polytechnic University, 30 Lenin Ave, Tomsk 634050, Russia

HIGHLIGHTS

- Single-atom Mo modified by 20 p-block elements as axial ligands was studied by first-principles calculation.
- The axial ligand had a significant effect on adsorption strength of Mo atom for CO_2RR intermediates.
- Ge-MoN_4 exhibited the best performance in the two-electron CO_2RR.
- The CO_2RR activity was related to the inherent properties of the axial ligands.

GRAPHICAL ABSTRACT

The p-block elements are evaluated as axial ligands of single-atom Mo for highly efficient two-electron CO_2 reduction reaction.

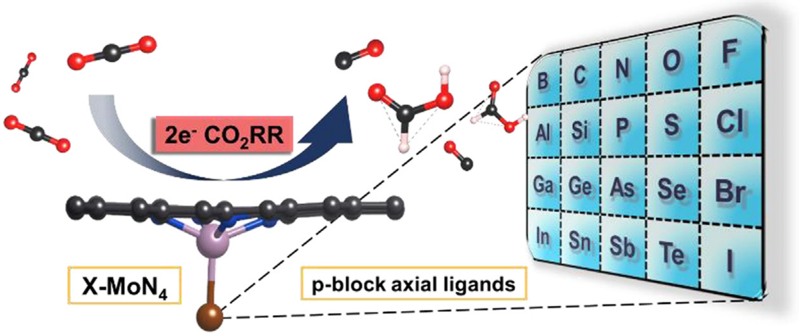

ARTICLE INFO

Article history:
Received 13 January 2023
Received in revised form 10 February 2023
Accepted 10 March 2023
Available online 16 March 2023

Keywords:
First-principles calculation
Molybdenum-nitrogen-carbon catalysts
P-block axial ligands
CO_2 reduction reactions
Orbital hybridization

ABSTRACT

Inspired by the structure of molybdenum-based metalloenzymes with high CO_2 conversion efficiency in nature, the catalytic performance of a series of modified MoN_4 for two-electron CO_2 reduction reaction (CO_2RR) was systematically studied using first-principles calculations. The effect of 20 p-block elements as axial ligands on the structure of MoN_4 was evaluated. Benefiting from the significant effect of the axial ligands on the adsorption strength of Mo for intermediates, both activity and selectivity were improved, especially Ge-MoN_4 exhibited the best performance in the formic acid (HCOOH) pathway. The orbital hybridization between Mo and the intermediate was weakened to varying degrees by axial ligands. Furthermore, the activity of the catalysts was related to the properties of the axial ligands, especially the Mo-N bond length and the electronegativity difference between Mo and the axial ligands. This work provides a thorough understanding and guidance for modifying the coordination environment of single-atom catalysts for CO_2RR.

---

* Corresponding authors.
E-mail addresses: dswang@zju.edu.cn (D. Wang), yhou@zju.edu.cn (Y. Hou).

https://doi.org/10.1016/j.ces.2023.118638
0009-2509/

1. Introduction

The excessive emission of CO_2 caused by the massive use of fossil energy has caused severe environmental problems (Gorbunov et al., 2022; Wang et al., 2022b; Wang et al., 2017; Wei et al., 2020), such as global warming and the increase in extreme climate. The conversion of CO_2 into fuels and chemicals with high value-added is a technology conducive to sustainable development and has been widely studied in recent years (Hu et al., 2022; Lee et al., 2018; Zheng et al., 2023). However, due to the inherent inertness of the C = O bond (Wang et al., 2022c; Wang et al., 2021d) and the competition of hydrogen evolution reaction (HER) in aqueous electrolyte (Chen et al., 2020a; Dou et al., 2019; Sun et al., 2021), catalysts with high activity and selectivity are needed to achieve efficient CO_2RR, which is still a great challenge.

With the decrease in the size of metal-based catalysts, their catalytic activity and selectivity will be further optimized (Geng et al., 2021; Liu et al., 2022; Wang et al., 2020). Because of the high specific surface area (Fu et al., 2022; Zhu et al., 2021), nearly 100% theoretical atom utilization (Gu et al., 2022; Wang et al., 2022d), and excellent activity (Chang et al., 2022; Li et al., 2022; Liu et al., 2022), single-atom catalysts (SACs) gained significant attention. Nitrogen-doped grapheme-supported atomic scale dispersed catalysts (TM-NC) for CO_2RR have been widely reported (Feng et al., 2020; Liu et al., 2020; Yuan et al., 2020; Zheng et al., 2021). Nevertheless, the focus of metal-active centers is on Cu (Chen et al., 2022; Creissen and Fontecave, 2022), Ni (Yang et al., 2020), Fe (Bonetto et al., 2020; Chen et al., 2022; Li et al., 2021), etc. The study of other kinds of metal-based SACs will help to explore the internal relationship between the structure and performance. For example, Cu SACs have been reported to be highly active for CO_2-RR due to their mild adsorption of intermediates and ability to facilitate C–C coupling and produce C_2 products (Xu et al., 2021). Compared with metallic Ni catalyst, atomically dispersed Ni SACs with characteristic electronic configurations are capable of lowering the energy barrier of CO_2 activation, especially unsaturated Ni-N sites (Zhang and Guan, 2020). And due to the strong interactions between isolated Fe atoms and N atoms from the support, the activity of FeN_4 sites is higher than Fe nanoparticles and single-atom Fe supported on N-free graphene (Zhang et al., 2018). This study presents promising opportunities for enhancing the commercial viability of CO_2RR and expanding the utilization of SACs in this field.

The SACs with earth-abundant Mo as active center have been widely selected as catalysts for nitrogen fixation (Ling et al., 2018; Xue et al., 2021) and hydrogen evolution reactions (Chen et al., 2017; Gao et al., 2019). Due to the half-filled, highly tunable 4d orbital electronic structure, the intrinsic catalytic performance of Mo-NC can be greatly improved by forming strong orbital hybridization with surrounding atoms to adjust the electronic structure of active sites (Chen et al., 2020b; Cheng et al., 2022; Ru et al., 2022). However, the Mo-NC materials used for CO_2RR catalysis are rarely reported because the strong adsorption of the Mo atom on CO will lead to the occurrence of poisoning (Wang et al., 2021c), which hinders the subsequent reaction. Mo-dependent formate dehydrogenases (FDHs) are a kind of Mo-based metalloenzymes existing in organisms in nature, which can effectively interconvert of CO_2 and formate (Robinson et al., 2020). As known, the strong interaction between the active center atoms and the surrounding coordination environment greatly affects the catalytic performance of SACs. Drawing inspiration from the structure of FDHs, it is expected that high CO_2RR performance can be generated by rationally designing the local coordination environment of Mo SACs (Chen et al., 2021; Pan et al., 2018; Rivera Cruz et al., 2021). However, to the best of our knowledge, focusing on the significant impact of the axial modification on the performance of 2D TM-NC catalysts has rarely been reported.

Considering the product's production cost and economic value, CO and formic acid generated through the two-electron reaction pathway are the two most commercially viable products for CO_2RR (Chen et al., 2018). Herein, using first-principles calculations based on density functional theory (DFT), a series of Mo SACs supported on N-doped graphene modified by axial ligands coordination were systematically investigated for the performance of CO_2RR. The ligands included 20 elements of the p-block in the first five periods. The adsorption strength of Mo atoms for reaction intermediates can be significantly regulated by the axial coordination, which can in turn alter the rate-determining step (RDS). For the formic acid pathway, the reaction energy of MoN_4 coordinated with Ge axially was as low as 0.50 eV. Further electronic structure analysis proved that the axial ligands optimized the electronic distribution of the Mo atom, reduced the hybridization with the 2p orbital of the *CO and *OCHO, and thus improved the activity and selectivity of Mo-based SACs. More importantly, an internal relationship between catalyst performance and ligand properties was found.

2. Computation method

All the periodic DFT calculations were performed using the plane wave Vienna Ab-Initio Simulation Package (VASP) code (Kresse and Furthmüller, 1996). The interaction between ions and core electrons was described by the projector augmented wave (PAW) potentials (Kresse and Joubert, 1999). The electron exchange–correlation energy was treated within the generalized gradient approximation (GGA) (Perdew and Wang, 1992) with the Perdew–Burke–Ernzerh (PBE) function (Perdew et al., 1996). A plane-wave basis set with a kinetic energy cutoff of 500 eV was used in all calculations. The convergence criteria for the electronic self-consistent iteration and force were set to 10^{-6} eV and 0.03 eV/Å, respectively. The Brillouin zone was sampled by a $2 \times 2 \times 1$ k-point grid with the Monkhorst–Pack scheme for geometric optimization and a $4 \times 4 \times 1$ for electronic structure calculation. The effect of van der Waals interaction was performed using the DFT-D3 functional (Grimme et al., 2010), and spin polarization was also considered.

The four-coordinate MoN_4 moiety was modulated as a Mo atom embedded in a periodic 5×5 graphene support with four N atoms doped, which contained 44C atoms, 4 N atoms, and 1 Mo atom. MoN_4 with an axial ligand was expressed as X-MoN_4, in which X represented the axial ligand. A vacuum thickness of 15 Å was set to avoid interactions periodically. All the models were fully relaxed in geometric optimization.

The binding energy (E_b) of axial ligand X was calculated based on Eq. (1):

$$E_b(X) = E(X - MoN_4) - E(MoN_4) - E(X) \tag{1}$$

where E(X-MoN_4), E(MoN_4), and E(X) were the total energies of the MoN_4 unit cell with axial ligand X, MoN_4 unit cell and axial ligand X, respectively. The state of the ligands is the most stable single substance state at room temperature (T = 298.15 K). The free Gibbs energy (G) of the reaction was calculated by Eq. (2):

$$G = E + ZPE - TS \tag{2}$$

here, E was the total energy obtained from DFT calculations, ZPE and S were the zero-point energy and entropy, respectively, and T = 298.15 K. The thermodynamic correction value was analyzed using VASPKIT (Wang et al., 2021b). The elementary step with the most positive Gibbs free-energy change (ΔG_{max}) was the potential-limiting step (PLS). The potential of PLS was defined as the limiting potential (U_L), which was an estimate of catalytic activity, and the value was calculated by Eq. (3):

$$U_L = -\Delta G_{max}/e \tag{3}$$

Display and modification of models and analysis of the charge density difference were conducted using the VESTA code (Momma and Izumi, 2008).

3. Results and discussion

3.1. Structures and stabilities

The original MoN_4 structure diagram is shown in Fig. 1a. Atomic Mo is coordinated with four pyridine N, which exhibited the best stability in Mo-NC SACs (Lou et al., 2022). The unique structure of N-doped graphene allows both sides of the carbon plane to interact with adsorbates, potentially enabling coordination with ligands in an axial direction. The structure models that result from axial coordination with p-block elements are shown in Fig. 1b and Fig. S1. Due to the introduction of the axial ligand X, the Mo-N bond length in the X-MoN_4 structure changed significantly, and the change in the bond length followed a specific pattern. As illustrated in Fig. 1d, within the same group, the Mo-N bond length decreased with increasing periods.

The binding energy (E_b) of axial ligand X on MoN_4 was calculated to evaluate the thermodynamic stability of X-MoN_4. It can be found from Fig. 1e that E_b in each group gradually became positive with increasing the number of periods. The O-MoN_4 had the most negative E_b (-5.36 eV), suggesting it had the most stable thermodynamic structure. In contrast, C, Si, B, and Al had positive E_b, indicating that their structures were unfavorable thermodynamically, which made them challenging to synthesize experimentally. Therefore, these four structures were not considered in the subsequent discussion.

3.2. Catalytical activity for the CO reaction pathway

CO_2RR has two reaction pathways through the two-electron mechanism, one product is CO and the other is formic acid. The initial steps of both pathways are CO_2 adsorption and activation combined with proton-electron coupling. For the CO generation pathway, the Gibbs free energy step diagram of the original MoN_4 is shown in Fig. S2. The generation of *COOH and *CO was exothermic, suggesting that both were spontaneous thermodynamic steps. It was speculated that the Mo atom was pushed out of the carbon plane and that the conical structure formed was beneficial to the stronger adsorption of small molecules due to its higher charge density (Lou et al., 2022). However, too strong adsorption for CO made Mo difficult to desorb, leading to CO poisoning and preventing the production of CO.

As for the sixteen kinds of MoN_4 structures with different axial ligands, their reaction thermodynamics changed significantly (Fig. S3). All the steps for generating *COOH on the reaction step became uphill, indicating that this reaction step was exothermic. And due to CO desorption becoming a spontaneous step, CO poisoning on X-MoN_4 was suppressed. This shows that the RDS has changed under the influence of axial ligands. More importantly, the RDS was transformed from a non-electrochemical reaction (CO desorption) to an electrochemically-controlled step, which allowed for the optimization of catalyst performance by adjusting the applied voltage (Guo et al., 2017), pH (Birdja et al., 2019), and other experimental conditions (Mao and Hatton, 2015). However, the maximum reaction Gibbs free energy (ΔG_{max}) values of most X-MoN_4 structures were higher than that of MoN_4 structures (Fig. 2a). Only two types of axial ligands coordinated structures (Ga-MoN_4 and In-MoN_4) required lower ΔG_{max} than that of MoN_4 (1.44 eV). Among all catalysis, In-MoN_4 required the lowest energy (1.14 eV). The above results suggested that the coordination of axial ligands could significantly adjust the adsorption strength of MoN_4 on reaction intermediates, thus changing the RDS of CO_2RR.

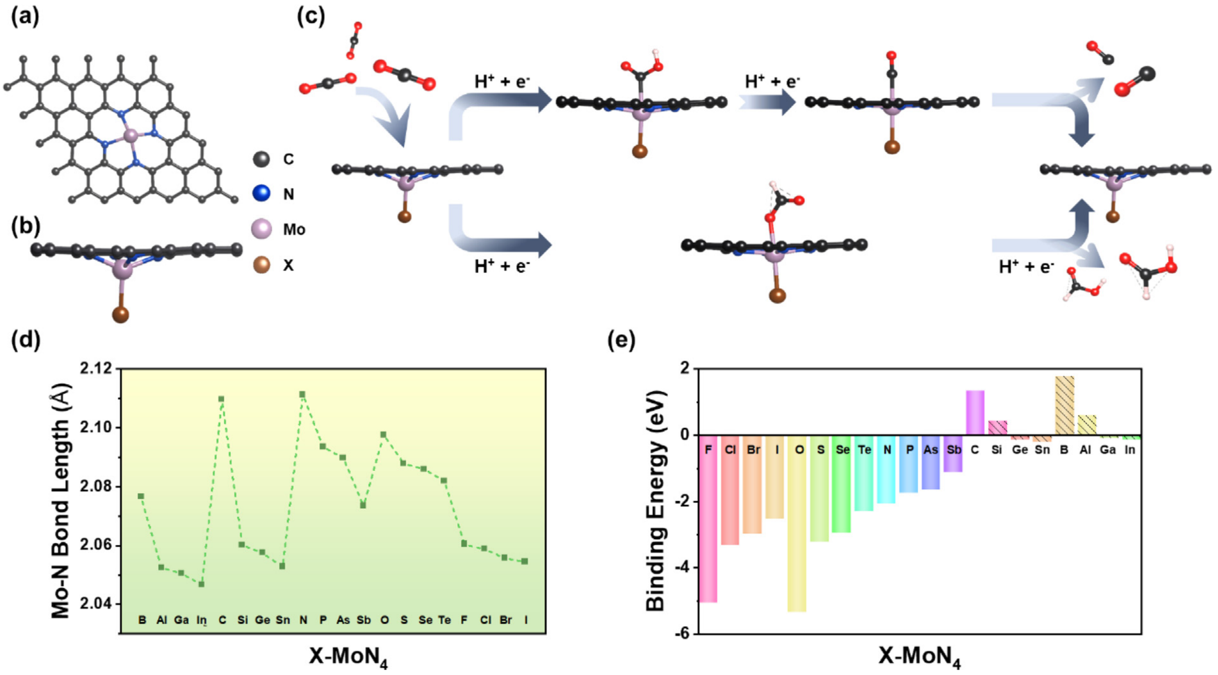

Fig. 1. (a) The model of original MoN_4 catalysts. (b) The model of axially coordinated X-MoN_4 catalysts. (c) Schematic diagram of the two-electron reaction pathway of CO_2RR. (d) The Mo-N bond length for different X-MoN_4 structures. (e) Binding energies of axially coordinated X-MoN_4 catalysts.

3.3. Catalytical activity for formic acid reaction pathway

Inspired by the results that the axial ligands can adjust the adsorption strength of intermediates, the effect of axial coordination on the reaction activity of MoN_4 was studied in the formic acid reaction pathway (Fig. S4). Similarly to the CO pathway, as compared with the strong adsorption of original MoN_4 in *OCHO (Fig. S5), the adsorption strength of MoN_4 with the axial ligand decreased obviously (Fig. S6). It is worth noting that the ΔG_{max} for the reaction pathway to formic acid of most X-MoN_4 was lower than that of MoN_4 (Fig. 2b), indicating that the axial coordination strategy effectively optimized the performance of the formic acid pathway. More importantly, the ΔG_{max} of Ge-MoN_4 was only 0.50 eV, much lower than that of MoN_4 (1.5 eV). These low free energies implied that the X-MoN_4 structure was more suitable for formic acid production. According to the Sabatier principle, the adsorption of a highly active catalyst on an intermediate is not too strong or too weak. (He et al., 2022; Wang et al., 2022a). From the plot with limiting potential ($U_L = -\Delta G_{max} / e$) vs. ΔG (*OCHO), it can be found that there was a volcanic relationship between them (Fig. 2c). The catalysts on the left side of the volcano plot had too strong adsorption for the intermediate *OCHO, which hindered its further reduction reaction. On the other hand, the CO_2RR activity of the catalysts located on the right side of the volcanic peak was limited by its weak affinity for *OCHO, which was not conducive to CO_2 adsorption and activation. Ge-MoN_4 was the catalyst closest to the volcanic peak with moderate adsorption strength, thus exhibiting the CO_2RR high-performance results.

Since the similar reaction potential, the HER reaction was a competitive reaction of CO_2RR (Cai et al., 2022; Wang et al., 2021a). The Gibbs free energy of HER of all X-MoN_4 catalysts was calculated (Fig. S7). Among them, N-MoN_4 and O-MoN_4 had the highest free energy for HER. In general, the difference value of $U_L(CO_2RR)$ and $U_L(HER)$ ($U_L(CO_2RR)$ - $U_L(HER)$) can be used to indicate the catalyst selectivity. The more positive the difference value, the weaker the HER competitiveness. Considering the adsorption capacity of small molecules and the application potential of catalysts, the difference values were calculated for part of X-MoN_4 with moderate adsorption capacity for *OCHO. As shown in Fig. 2d, the calculated structures all had large positive values, indicating that they all had a strong selectivity for CO_2RR. The summary of the reaction energy of the three reaction paths is shown in Fig. 2e, which intuitively shows that the axial ligand X can effectively regulate the adsorption capacity of MoN_4 for intermediates, thereby improving its catalytic activity and selectivity for CO_2RR.

3.4. Mechanism and correlation of X-MoN_4 for CO_2RR

To further explore the reason why axial ligands change the RDS of Mo-based SACs, the projected density of states (PDOS) was calculated and analyzed. For MoN_4 (Fig. S8), continuous states near the Fermi level indicate its good conductivity. In addition, a strong d orbital peak near the Fermi level contributes a large number of active d electrons that can participate in chemical reactions. From the PDOS diagram of MoN_4 with *CO adsorbed (Fig. 3a), it can be seen that the 4d orbital of Mo and the 2p orbital of CO passed through the Fermi energy level and had a large overlap. It means that a strong d-p orbital hybridization occurred between Mo and CO, especially between the d_{xz} orbital of Mo and the p_x orbital of CO, resulting in a strong adsorption capability to CO. In contrast, on the PDOS diagram of In-MoN_4 (Fig. 3a), the hybridization between the 4d orbital of Mo and the 2p orbital of CO near the Fermi level was much weaker, suggesting that In-MoN_4 could weaken the excessive adsorption of CO and avoid being poisoned.

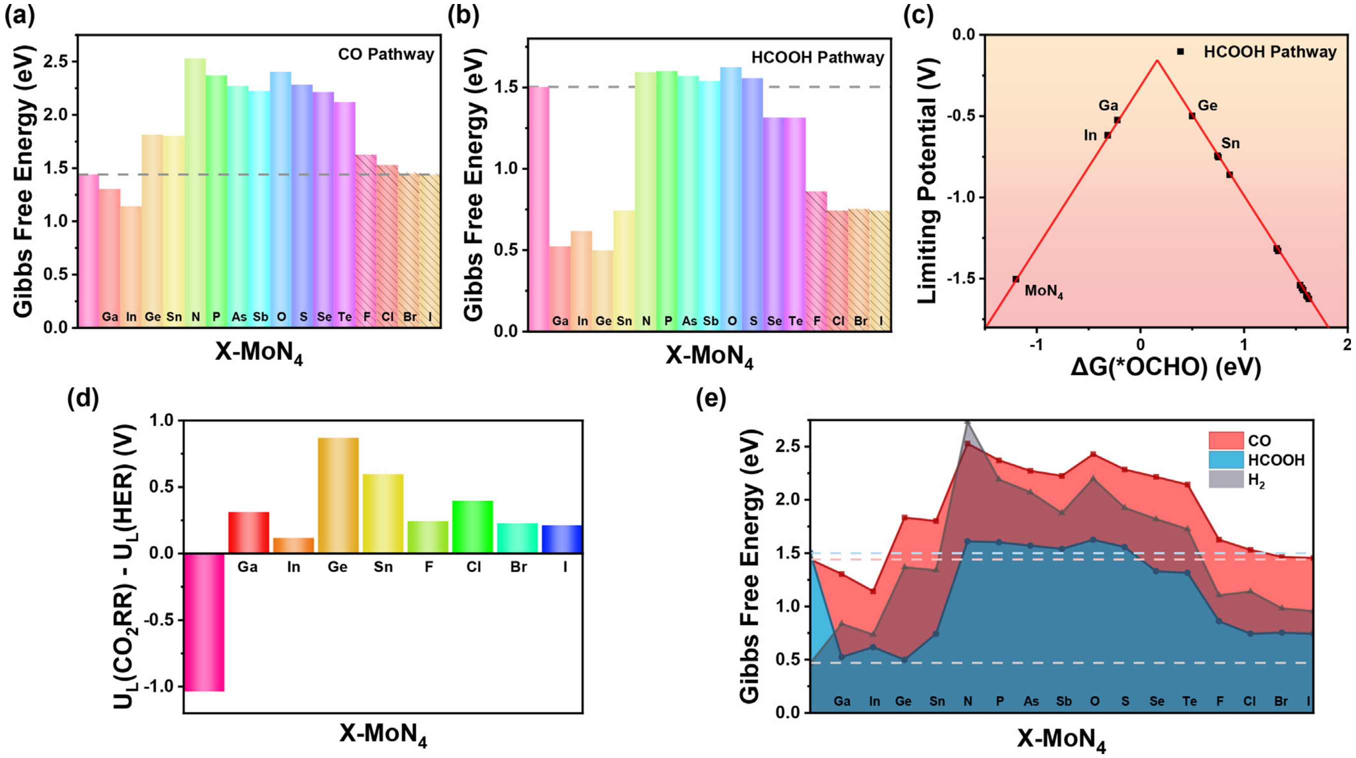

Fig. 2. The ΔG_{max} for (a) CO pathway and (b) formic acid pathway of MoN_4 and X-MoN_4, where the dash line represents the data of MoN_4. (c) A volcano plot for the limiting potential against the free energy ΔG(*OCHO) on MoN_4 and X-MoN_4 catalysts. (d) Limiting potential difference value of MoN_4 and X-MoN_4 for CO_2RR and HER. (e) The summary of the ΔG_{max} of MoN_4 and X-MoN_4 for CO pathway, formic acid pathway and HER, where the blue dash line, pink dash line, and grey dash line stand for the data of MoN_4 for formic acid pathway, CO pathway, and HER, respectively. (For interpretation of the references to colour in this figure legend, the reader is referred to the web version of this article.)

This conclusion can also be drawn from the PDOS of other X-MoN_4 (Fig. S9). Therefore, the decrease in the affinity for CO can be attributed to the effective regulation of the Mo electronic structure by introducing axial ligands. Similarly, the DOS of MoN_4 adsorbed with *OCHO intermediate was also calculated to deeply understand the important role of axial ligands. Consistent with the previous conclusion, compared to the original MoN_4, the 4d orbital of Mo of X-MoN_4 at the Fermi level overlaps less with the 2p orbital of *OCHO, with the main overlaps being far away from the Fermi level (Fig. 3b and Fig. S10). The ability of the axial ligands to adjust the electronic configuration has also been confirmed in previous work (Wang et al., 2021e). It is worth noting that the spin-down d orbital of the Mo atom seems to have a greater impact on the adsorption energy. The weaker electronic interaction between the active site and the reaction intermediate solved the problem of strong adsorption strength and greatly improved catalytic activity.

The catalytic performance of the catalyst is closely related to the electronic structure of its active center. To understand the mechanism of different adsorption capacities of Mo atoms under the influence of axial ligands, the charge density difference analysis and Bader charge analysis were conducted for MoN_4 and X-MoN_4. In the MoN_4 structure, the electron of Mo depleted and Mo had a positive charge property (Fig. S11). After axial coordination with the ligands, electron redistribution occurred between the ligands X and Mo to different degrees. The charge accumulation occurred on all ligands except Ga, In, Ge, and Sn (Fig. 3c). It is worth noting that such results are in good agreement with the difference in the adsorption configuration of *OCHO. Considering that MoN_4 modified by these four ligands had the best catalytic performance, it can be inferred that the ability of the ligand to transfer electrons had a significant regulatory effect on the adsorption capacity of Mo. The ligands with a strong electron-gaining property interacted with the Mo atom too strongly, thus excessively weakening the adsorption strength of Mo for intermediates. The appropriate ability to gain and lose electrons can reasonably optimize the electronic level of the Mo atom, generating moderate d-p interaction. This explained the underlying reason for the appearance of the previous volcano plot. It can also be proved by the fact that the degree of electron loss of the Mo atom varied according to the difference in the properties of ligands (Fig. S12), which was speculated to be related to the difference value of electronegativity between Mo and X ($\Delta\chi = \chi_{Mo} - \chi_X$) (Fig. 3d). After the reaction intermediate *OCHO was adsorbed, electrons were accumulated in the adsorbed group and depleted on the Mo atom, which indicated that electrons were transferred from Mo to the intermediates (Fig. S13).

It is of great significance to find the internal relationship between the catalytic activity and the inherent properties of the catalyst. First, taking the average length of the Mo-N bond as a variable, it can be found that it had a linear correlation with ΔG_{max} not only for the CO pathway (Fig. 4a) but also for the formic acid pathway (Fig. 4b). Therefore, it can be proved that the catalytic capacity of CO_2RR can be roughly judged according to the bond length, which is an attribute of the structure itself. According to previous reports, electronegativity may be a key parameter in the study of ligand-substrate interactions (Lu et al., 2022). It was proposed here to use the difference value of the electronegativity ($\Delta\chi$) to establish a relationship with the thermodynamic properties of the catalysts. As we can see from Fig. S14, the number of electrons transferred by ligands was related to the number of electrons transferred by Mo. And the number of electrons transferred in Mo increased with the increase of $\Delta\chi$ (Fig. 3d). This also agreed with the physical meaning of electronegativity. It is crucial to note that by grouping the four electron-donating ligands into one group and the remaining 12 ligands into three groups based on their position in the periodic table, a better understanding can be gained about the relationship between the Gibbs free energy of key reaction steps (i.e. $\Delta G(^*COOH)$ in the CO pathway and $\Delta G(^*OCHO)$ in the formic acid pathway) and $\Delta\chi$ for each group. For both the

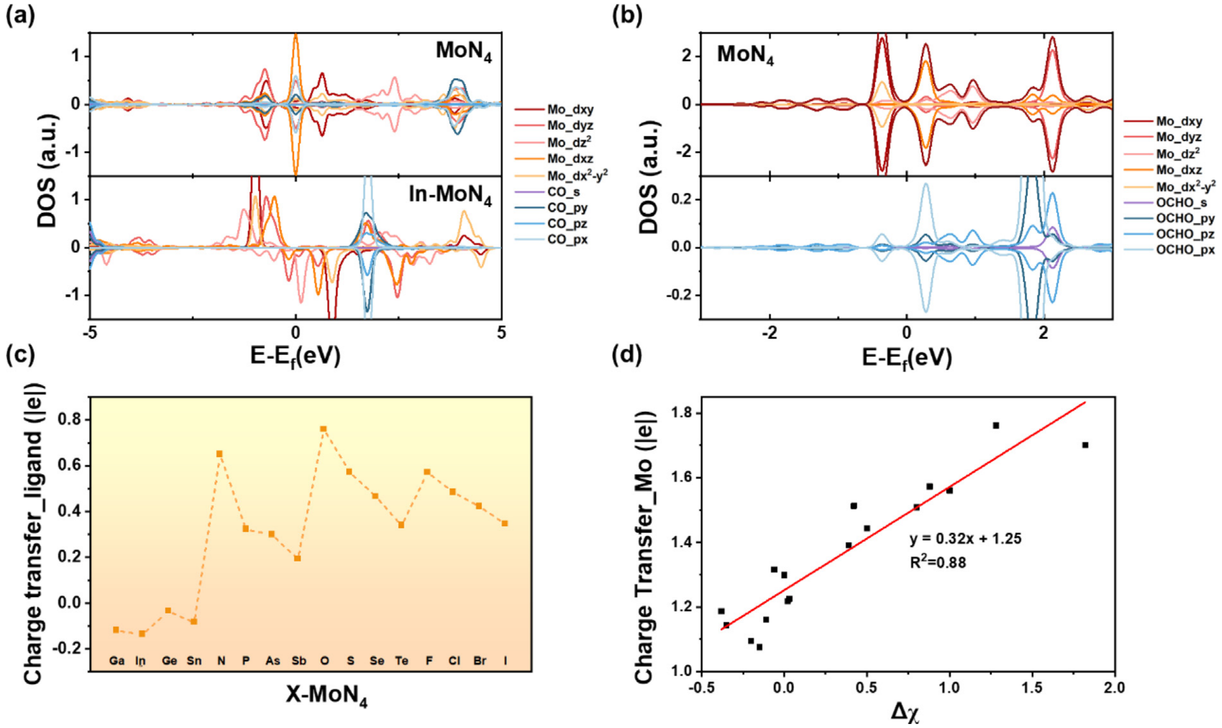

Fig. 3. (a) Comparison between PDOS of MoN_4 and In-MoN_4 with CO adsorbed. (b) Calculated PDOS of d orbital of Mo and s, p orbital of *OCHO of MoN_4. (c) The number of charge transfer of axial ligand of X-MoN_4, which negative value represent electron loss and positive value represent electron gain. (d) The linear relations of the number of charge transfer of the Mo atoms vs. difference value of electronegativity.

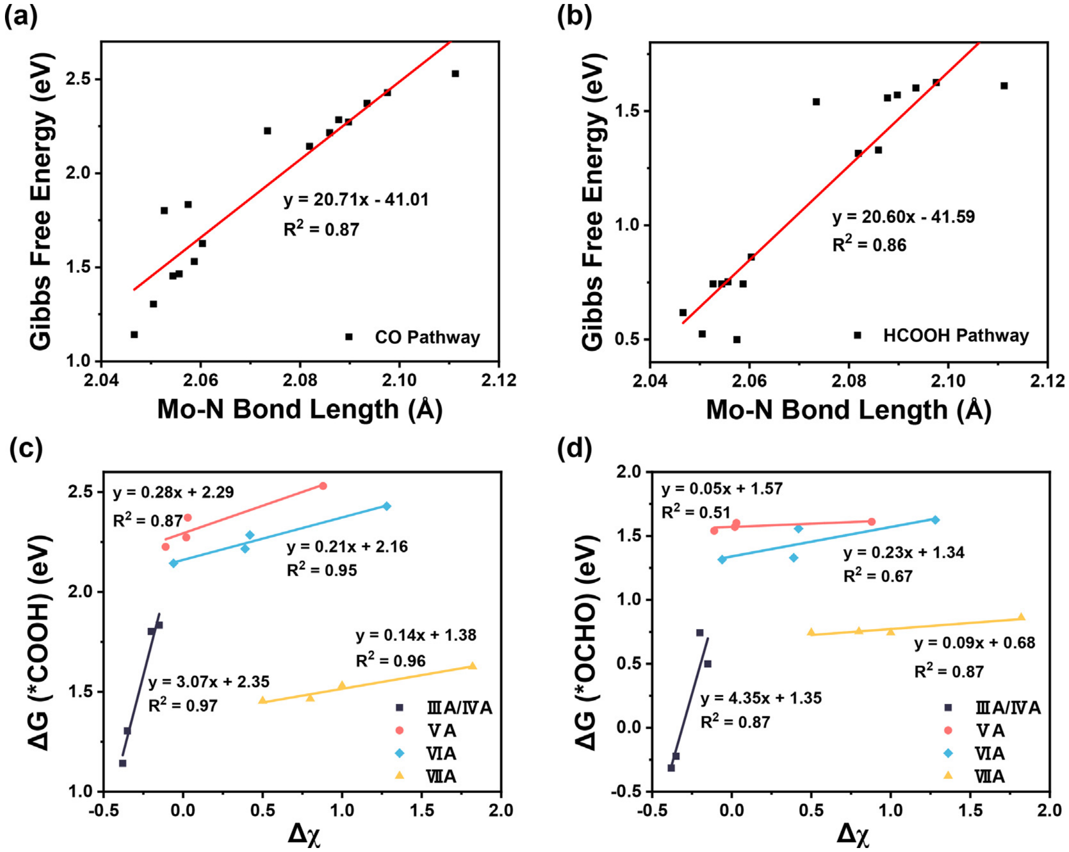

Fig. 4. The scaling relations of ΔG_{max} of X-MoN_4 for (a) CO pathway and (b) formic acid pathway vs. the length of Mo-N bond. The linear relations of (c) ΔG(*COOH) and (d) ΔG(*OCHO) vs. difference value of electronegativity between Mo and X.

CO reaction pathway (Fig. 4c) and the formic acid reaction pathway (Fig. 4d), the linear relationship of each group was in good agreement with $\Delta\chi$. This also proved that the electronegativity difference between the ligands and the central metal atom could be used as a simple and practical descriptor to measure the catalytic activity of a five-coordinated single atom with an axial ligand. In general, we found the influence law of axial coordination on the catalytical performance of SACs, which provided theoretical guidance for the design of MoN_4 and other TM-NC materials.

4. Conclusion

In this work, 20 elements in the p-block were used as axial ligands to modify the structure of MoN_4, and a series of five coordinated X-MoN_4 SACs were designed for two-electron CO_2RR. Theoretical calculations revealed that axial coordination has a significant impact on regulating the Mo atom's adsorption capacity for reaction intermediates. In-MoN_4 had the best catalytic performance (1.14 V) in the CO pathway. For the formic acid reaction pathway, Ge-MoN_4 exhibited the lowest U_L value (0.5 V) among the studied axially coordinated structures. The electronic structure analysis demonstrated that by adjusting the electronic structure of the d orbital of Mo, the axial ligands could reduce the hybridization of the 4d orbital of Mo and the 2p orbital of the intermediate, achieving a moderate adsorption strength. Further data analysis proved that there was an internal relationship between performance and the properties of ligands, especially there was a nearly linear relationship between U_L and $\Delta\chi$ in each group. This study offers theoretical guidance for simultaneously improving the activity and selectivity of MoN_4 in CO_2RR and presents new ideas for strategically engineering the coordination environment of SACs.

CRediT authorship contribution statement

Yingnan Liu: Conceptualization, Methodology, Software, Formal analysis, Writing – original draft. **Dashuai Wang:** Software, Resources, Writing – review & editing, Supervision, Funding acquisition. **Bin Yang:** Writing – review & editing. **Zhongjian Li:** Writing – review & editing. **Xianyun Peng:** Writing – review & editing. **Zhibin Liu:** Writing – review & editing. **Libin Zeng:** Writing – review & editing. **Tao Zhang:** Writing – review & editing. **Raul D. Rodriguez:** Writing – review & editing. **Lecheng Lei:** Writing – review & editing. **Yang Hou:** Resources, Writing – review & editing, Funding acquisition.

Data availability

Data will be made available on request.

Declaration of Competing Interest

The authors declare that they have no known competing financial interests or personal relationships that could have appeared to influence the work reported in this paper.

Acknowledgements

This work was jointly supported by the National Natural Science Foundation of China (U22A20432, 22278364, 22211530045, 22178308), the development project of Zhejiang Province's "Jianbing" and "Lingyan" (2023C01226), National Key Research and Development Program of China (2022YFB4002100), the Fundamental Research Funds for the Central Universities

(226-2022-00044, 226-2022-00055), the Startup Foundation for Hundred-Talent Program of Zhejiang University. The authors greatly acknowledge the financial support from the Research Funds of Institute of Zhejiang University-Quzhou (IZQ2021RCZX040, IZQ2021KJ2003) and Guangdong Basic and Applied Basic Research Foundation (No. 2020A1515110338)

Appendix A. Supplementary data

Supplementary data to this article can be found online at https://doi.org/10.1016/j.ces.2023.118638.

References

Birdja, Y.Y., Pérez-Gallent, E., Figueiredo, M.C., Göttle, A.J., Calle-Vallejo, F., Koper, M.T.M., 2019. Advances and challenges in understanding the electrocatalytic conversion of carbon dioxide to fuels. Nat. Energy 4, 732–745.

Bonetto, R., Crisanti, F., Sartorel, A., 2020. Carbon dioxide reduction mediated by iron catalysts: mechanism and intermediates that guide selectivity. ACS Omega 5, 21309–21319.

Cai, C., Liu, K., Zhu, Y., Li, P., Wang, Q., Liu, B., Chen, S., Li, H., Zhu, L., Li, H., Fu, J., Chen, Y., Pensa, E., Hu, J., Lu, Y.-R., Chan, T.-S., Cortés, E., Liu, M., 2022. Optimizing hydrogen binding on Ru sites with RuCo alloy nanosheets for efficient alkaline hydrogen evolution. Angew. Chem., Int. Ed. 61, e202113664.

Chang, Q., Liu, Y., Lee, J.H., Ologunagba, D., Hwang, S., Xie, Z., Kattel, S., Lee, J.H., Chen, J.G., 2022. Metal-coordinated phthalocyanines as platform molecules for understanding isolated metal sites in the electrochemical reduction of CO_2. J. Am. Chem. Soc. 144, 16131–16138.

Chen, H., Chen, J., Si, J., Hou, Y., Zheng, Q., Yang, B., Li, Z., Gao, L., Lei, L., Wen, Z., Feng, X., 2020a. Ultrathin tin monosulfide nanosheets with the exposed (001) plane for efficient electrocatalytic conversion of CO_2 into formate. Chem. Sci. 11, 3952–3958.

Chen, Z., Huang, A., Yu, K., Cui, T., Zhuang, Z., Liu, S., Li, J., Tu, R., Sun, K., Tan, X., Zhang, J., Liu, D., Zhang, Y., Jiang, P., Pan, Y., Chen, C., Peng, Q., Li, Y., 2021. Fe_1N_4-O_1 site with axial Fe-O coordination for highly selective CO_2 reduction over a wide potential range. Energy Environ. Sci. 14, 3430–3437.

Chen, C., Khosrowabadi Kotyk, J.F., Sheehan, S.W., 2018. Progress toward commercial application of electrochemical carbon dioxide reduction. Chem 4, 2571–2586.

Chen, K., Liu, K., An, P., Li, H., Lin, Y., Hu, J., Jia, C., Fu, J., Li, H., Liu, H., Lin, Z., Li, W., Li, J., Lu, Y.-R., Chan, T.-S., Zhang, N., Liu, M., 2020b. Iron phthalocyanine with coordination induced electronic localization to boost oxygen reduction reaction. Nat. Commun. 11, 4173.

Chen, W., Pei, J., He, C.T., Wan, J., Ren, H., Zhu, Y., Wang, Y., Dong, J., Tian, S., Cheong, W.C., Lu, S., Zheng, L., Zheng, X., Yan, W., Zhuang, Z., Chen, C., Peng, Q., Wang, D., Li, Y., 2017. Rational design of single molybdenum atoms anchored on N-doped carbon for effective hydrogen evolution reaction. Angew. Chem. Int. Ed. Engl. 56, 16086–16090.

Chen, J., Wang, T., Wang, X., Yang, B., Sang, X., Zheng, S., Yao, S., Li, Z., Zhang, Q., Lei, L., Xu, J., Dai, L., Hou, Y., 2022. Promoting electrochemical CO_2 reduction via boosting activation of adsorbed intermediates on iron single-atom catalyst. Adv. Funct. Mater. 32, 2110174.

Cheng, C.-C., Yeh, Y.-X., Ting, Y.-C., Lin, S.-H., Sasaki, K., Choi, Y., Lu, S.-Y., 2022. Modulation of the coordination environment enhances the electrocatalytic efficiency of Mo single atoms toward water splitting. J. Mater. Chem. A 10, 8784–8797.

Creissen, C.E., Fontecave, M., 2022. Keeping sight of copper in single-atom catalysts for electrochemical carbon dioxide reduction. Nat. Commun. 13, 2280.

Dou, S., Song, J., Xi, S., Du, Y., Wang, J., Huang, Z.F., Xu, Z.J., Wang, X., 2019. Boosting electrochemical CO_2 reduction on metal-organic frameworks via ligand doping. Angew. Chem. Int. Ed. Engl. 58, 4041–4045.

Feng, J., Gao, H., Zheng, L., Chen, Z., Zeng, S., Jiang, C., Dong, H., Liu, L., Zhang, S., Zhang, X., 2020. A Mn-N_3 single-atom catalyst embedded in graphitic carbon nitride for efficient CO_2 electroreduction. Nat. Commun. 11, 4341.

Fu, N., Liang, X., Li, Z., Li, Y., 2022. Single-atom site catalysts based on high specific surface area supports. Phys. Chem. Chem. Phys. 24, 17417–17438.

Gao, X., Zhou, Y., Tan, Y., Yang, B., Cheng, Z., Shen, Z., 2019. Single Mo atoms supported on N-doped carbon with N/C edge-site for enhanced electrochemical hydrogen evolution. Int. J. Hydrogen Energy 44, 14861–14868.

Geng, J., Zhang, S., Xu, H., Wang, G., Zhang, H., 2021. An oxygen-coordinated molybdenum single atom catalyst for efficient electrosynthesis of ammonia. Chem. Commun. 57, 5410–5413.

Gorbunov, D.N., Nenasheva, M.V., Terenina, M.V., Kardasheva, Y.S., Kardashev, S.V., Naranov, E.R., Bugaev, A.L., Soldatov, A.V., Maximov, A.L., Karakhanov, E.A., 2022. Transformations of carbon dioxide under homogeneous catalysis conditions (a review). Pet. Chem. 62, 1–39.

Grimme, S., Antony, J., Ehrlich, S., Krieg, H., 2010. A consistent and accurate ab initio parametrization of density functional dispersion correction (DFT-D) for the 94 elements H-Pu. J. Chem. Phys. 132, 154104.

Gu, Y., Xi, B.J., Zhang, H., Ma, Y.C., Xiong, S.L., 2022. Activation of main-group antimony atomic sites for oxygen reduction catalysis. Angew. Chem., Int. Ed. Engl. 61, e202202200.

Guo, R.-H., Liu, C.-F., Wei, T.C., Hu, C.-C., 2017. Electrochemical behavior of CO_2 reduction on palladium nanoparticles: Dependence of adsorbed CO on electrode potential. Electrochem. Commun. 80, 24–28.

He, F., Zhao, Y., Yang, X., Zheng, S., Yang, B., Li, Z., Kuang, Y., Zhang, Q., Lei, L., Qiu, M., Dai, L., Hou, Y., 2022. Metal-organic frameworks with assembled bifunctional microreactor for charge modulation and strain generation toward enhanced oxygen electrocatalysis. ACS Nano 16, 9523–9534.

Hu, X., Liu, Y., Cui, W., Yang, X., Li, J., Zheng, S., Yang, B., Li, Z., Sang, X., Li, Y., Lei, L., Hou, Y., 2022. Boosting industrial-level CO_2 electroreduction of N-doped carbon nanofibers with confined tin-nitrogen active sites via accelerating proton transport kinetics. Adv, Funct. Mater., p. 2208781.

Kresse, G., Furthmüller, J., 1996. Efficient iterative schemes for ab initio total-energy calculations using a plane-wave basis set. Phys. Rev. B 54, 11169–11186.

Kresse, G., Joubert, D., 1999. From ultrasoft pseudopotentials to the projector augmented-wave method. Phys. Rev. B 59, 1758–1775.

Lee, W., Kim, Y.E., Youn, M.H., Jeong, S.K., Park, K.T., 2018. Catholyte-free electrocatalytic CO_2 reduction to formate. Angew. Chem. Int. Ed. Engl. 57, 6883–6887.

Li, Y., Ji, Y., Zhao, Y., Chen, J., Zheng, S., Sang, X., Yang, B., Li, Z., Lei, L., Wen, Z., Feng, X., Hou, Y., 2022. Local spin-state tuning of iron single-atom electrocatalyst by S-coordinated doping for kinetics-boosted ammonia synthesis. Adv. Mater. 34, 2202240.

Li, Z., Zeng, Q., Ye, Z., Zheng, W., Sang, X., Dong, C.-L., Yang, B., Pardiwala, S., Lu, J., Lei, L., Wu, G., Hou, Y., 2021. An integrated bioelectrochemical system coupled CO_2 electroreduction device based on atomically dispersed iron electrocatalysts. Nano Energy 87, 106187.

Ling, C., Bai, X., Ouyang, Y., Du, A., Wang, J., 2018. Single molybdenum atom anchored on N-doped carbon as a promising electrocatalyst for nitrogen reduction into ammonia at ambient conditions. J. Phys. Chem. C 122, 16842–16847.

Liu, K., Fu, J., Lin, Y., Luo, T., Ni, G., Li, H., Lin, Z., Liu, M., 2022. Insights into the activity of single-atom Fe-N-C catalysts for oxygen reduction reaction. Nat. Commun. 13, 2075.

Liu, J., Kong, X., Zheng, L., Guo, X., Liu, X., Shui, J., 2020. Rare earth single-atom catalysts for nitrogen and carbon dioxide reduction. ACS Nano 14, 1093–1101.

Lou, Z., Li, W., Yuan, H., Hou, Y., Yang, H., Wang, H., 2022. Structural rule of n-coordinated single-atom catalysts for electrochemical CO_2 reduction. J. Mater. Chem. A 10, 3585–3594.

Lu, R., Quan, C., Zhang, C., He, Q., Liao, X., Wang, Z., Zhao, Y., 2022. Establishing a theoretical insight for penta-coordinated iron-nitrogen-carbon catalysts toward oxygen reaction. Nano Res. 15, 6067–6075.

Mao, X., Hatton, T.A., 2015. Recent advances in electrocatalytic reduction of carbon dioxide using metal-free catalysts. Ind. Eng. Chem. Res. 54, 4033–4042.

Momma, K., Izumi, F., 2008. Vesta: A three-dimensional visualization system for electronic and structural analysis. J. Appl. Crystallogr. 41, 653–658.

Pan, Y., Lin, R., Chen, Y., Liu, S., Zhu, W., Cao, X., Chen, W., Wu, K., Cheong, W.C., Wang, Y., Zheng, L., Luo, J., Lin, Y., Liu, Y., Liu, C., Li, J., Lu, Q., Chen, X., Wang, D., Peng, Q., Chen, C., Li, Y., 2018. Design of single-atom Co-N_5 catalytic site: A robust electrocatalyst for CO_2 reduction with nearly 100% co selectivity and remarkable stability. J. Am. Chem. Soc. 140, 4218–4221.

Perdew, J.P., Burke, K., Ernzerhof, M., 1996. Generalized gradient approximation made simple. Phys. Rev. Lett. 77, 3865–3868.

Perdew, J.P., Wang, Y., 1992. Accurate and simple analytic representation of the electron-gas correlation energy. Phys. Rev. B 45, 13244–13249.

Rivera Cruz, K.E., Liu, Y., Soucy, T.L., Zimmerman, P.M., McCrory, C.C.L., 2021. Increasing the CO_2 reduction activity of cobalt phthalocyanine by modulating the σ-donor strength of axially coordinating ligands. ACS Catal. 11, 13203–13216.

Robinson, W.E., Bassegoda, A., Blaza, J.N., Reisner, E., Hirst, J., 2020. Understanding how the rate of C-H bond cleavage affects formate oxidation catalysis by a Mo-dependent formate dehydrogenase. J. Am. Chem. Soc. 142, 12226–12236.

Ru, S., He, M., Zhou, Y., Xu, C., Luo, Q., Yang, J., 2022. Theoretical and comparative analysis of graphdiyne and confined flexible nitrogen-doped graphdiyne-supported single-atom catalysts for electrochemical nitrogen reduction. J. Phys. Chem. C 126, 18282–18291.

Sun, X., Tuo, Y., Ye, C., Chen, C., Lu, Q., Li, G., Jiang, P., Chen, S., Zhu, P., Ma, M., Zhang, J., Bitter, J.H., Wang, D., Li, Y., 2021. Phosphorus induced electron localization of single iron sites for boosted CO_2 electroreduction reaction. Angew. Chem. Int. Ed. Engl. 60, 23614–23618.

Wang, X., Feng, S., Lu, W., Zhao, Y., Zheng, S., Zheng, W., Sang, X., Zheng, L., Xie, Y., Li, Z., Yang, B., Lei, L., Wang, S., Hou, Y., 2021d. A new strategy for accelerating dynamic proton transfer of electrochemical CO_2 reduction at high current densities. Adv. Funct. Mater. 31, 2104243.

Wang, W., Gao, Y., Li, H., Tian, F., Li, D., Cui, T., 2021c. Unraveling electrochemical CO reduction of the single-atom transition metals supported on N-doped phosphorene. Appl. Surf. Sci. 545, 148953.

Wang, Q., Liu, K., Fu, J., Cai, C., Li, H., Long, Y., Chen, S., Liu, B., Li, H., Li, W., Qiu, X., Zhang, N., Hu, J., Pan, H., Liu, M., 2021a. Atomically dispersed s-block magnesium sites for electroreduction of CO_2 to CO. Angew. Chem. Int. Ed. 60, 25241–25245.

Wang, Q., Liu, K., Hu, K., Cai, C., Li, H., Li, H., Herran, M., Lu, Y.-R., Chan, T.-S., Ma, C., Fu, J., Zhang, S., Liang, Y., Cortés, E., Liu, M., 2022b. Attenuating metal-substrate conjugation in atomically dispersed nickel catalysts for electroreduction of CO_2 to CO. Nat. Commun. 13, 6082.

Wang, T., Sang, X., Zheng, W., Yang, B., Yao, S., Lei, C., Li, Z., He, Q., Lu, J., Lei, L., Dai, L., Hou, Y., 2020. Gas diffusion strategy for inserting atomic iron sites into graphitized carbon supports for unusually high-efficient CO_2 electroreduction and high-performance Zn-CO_2 batteries. Adv. Mater. 32, 2002430.

Wang, X., Wang, Y., Sang, X., Zheng, W., Zhang, S., Shuai, L., Yang, B., Li, Z., Chen, J., Lei, L., Adli, N.M., Leung, M.K.H., Qiu, M., Wu, G., Hou, Y., 2021e. Dynamic activation of adsorbed intermediates via axial traction for the promoted electrochemical CO_2 reduction. Angew. Chem. Int. Ed. Engl. 60, 4192–4198.

Wang, X., An, Y., Liu, L., Fang, L., Liu, Y., Zhang, J., Qi, H., Heine, T., Li, T., Kuc, A., Yu, M., Feng, X., 2022d. Atomically dispersed pentacoordinated-zirconium catalyst with axial oxygen ligand for oxygen reduction reaction. Angew. Chem., Int. Ed. Engl. 61, e202209746.

Wang, K., Wang, Y., Yang, B., Li, Z., Qin, X., Zhang, Q., Lei, L., Qiu, M., Wu, G., Hou, Y., 2022a. Highly active ruthenium sites stabilized by modulating electron-feeding for sustainable acidic oxygen-evolution electrocatalysis. Energy Environ. Sci. 15, 2356–2365.

Wang, R., Wang, X., Weng, W., Yao, Y., Kidkhunthod, P., Wang, C., Hou, Y., Guo, J., 2022c. Proton/electron donors enhancing electrocatalytic activity of supported conjugated microporous polymers for CO_2 reduction. Angew. Chem., Int. Ed. Engl. 61, e202115503.

Wang, V., Xu, N., Liu, J.-C., Tang, G., Geng, W.-T., 2021b. VASPKIT: A user-friendly interface facilitating high-throughput computing and analysis using VASP code. Comput. Phys. Commun. 267, 108033.

Wang, W., Zhou, M., Yuan, D., 2017. Carbon dioxide capture in amorphous porous organic polymers. J. Mater. Chem. A 5, 1334–1347.

Wei, F., Wang, T., Jiang, X., Ai, Y., Cui, A., Cui, J., Fu, J., Cheng, J., Lei, L., Hou, Y., Liu, S., 2020. Controllably engineering mesoporous surface and dimensionality of SnO_2 toward high-performance CO_2 electroreduction. Adv. Funct. Mater. 30, 2002092.

Xu, C., Vasileff, A., Zheng, Y., Qiao, S.-Z., 2021. Recent progress of 3d transition metal single-atom catalysts for electrochemical CO_2 reduction. Adv. Mater. Interfaces 8, 2001904.

Xue, Z., Zhang, X., Qin, J., Liu, R., 2021. Anchoring Mo on C_9N_4 monolayers as an efficient single atom catalyst for nitrogen fixation. J. Energy Chem. 57, 443–450.

Yang, H., Lin, Q., Zhang, C., Yu, X., Cheng, Z., Li, G., Hu, Q., Ren, X., Zhang, Q., Liu, J., He, C., 2020. Carbon dioxide electroreduction on single-atom nickel decorated carbon membranes with industry compatible current densities. Nat. Commun. 11, 593.

Yuan, H., Li, Z., Zeng, X.C., Yang, J., 2020. Descriptor-based design principle for two-dimensional single-atom catalysts: carbon dioxide electroreduction. J. Phys. Chem. C 11, 3481–3487.

Zhang, Q., Guan, J., 2020. Single-atom catalysts for electrocatalytic applications. Adv. Funct. Mater. 30, 2000768.

Zhang, C., Yang, S., Wu, J., Liu, M., Yazdi, S., Ren, M., Sha, J., Zhong, J., Nie, K., Jalilov, A. S., Li, Z., Li, H., Yakobson, B.I., Wu, Q., Ringe, E., Xu, H., Ajayan, P.M., Tour, J.M., 2018. Electrochemical CO_2 reduction with atomic iron-dispersed on nitrogen-doped graphene. Adv. Energy Mater. 8, 1703487.

Zheng, W., Wang, Y., Shuai, L., Wang, X., He, F., Lei, C., Li, Z., Yang, B., Lei, L., Yuan, C., Qiu, M., Hou, Y., Feng, X., 2021. Highly boosted reaction kinetics in carbon dioxide electroreduction by surface-introduced electronegative dopants. Adv. Funct. Mater. 31, 2008146.

Zheng, W., Wang, D., Zhang, Y., Zheng, S., Yang, B., Li, Z., Rodriguez, R.D., Zhang, T., Lei, L., Yao, S., Hou, Y., 2023. Promoting industrial-level CO_2 electroreduction kinetics via accelerating proton feeding on a metal-free aerogel electrocatalyst. Nano Energy 105, 107980.

Zhu, Y., Miyake, K., Shu, Y., Moroto, K., Hirota, Y., Uchida, Y., Tanaka, S., Zheng, T., Katayama, M., Inada, Y., Morallón, E., Cazorla-Amorós, D., Kong, C.Y., Nishiyama, N., 2021. Single atomic Co coordinated with N in microporous carbon for oxygen reduction reaction obtained from Co/2-methylimidazole anchored to y zeolite as a template. Mater. Today Chem. 20, 100410.